Multi-objective optimization of a hybrid excitation generator with a parallel magnetic circuit based on the coupling of dual optimization algorithms

Tingjun Sun[1], Wenjing Hu[2✉], Fanxi Meng[1], Jinke Wu[1],
Yixin Liu[2], Huihui Geng[2], Weitao Liu[2], Wei Wang[2]

[1]*Shandong Remote Bento New Energy Vehicle Co*
Taian 271200, China

[2]*School of Transportation and Vehicle Engineering, Shandong University of Technology*
Zibo 255000, China

e-mail: *13853396897/@139.com, {✉ huwenjing/huihuigeng}@sdut.edu.cn,*
{2301275399@qq/964365822}@qq.com, {wjk66966@163/liuyixin20231}@163.com

Abstract: The coaxial parallel magnetic circuit dual-rotor hybrid excitation structure generator exhibits several advantages, including high output performance, a wide adjustment range, and excellent stability. This study introduces a topology for a parallel magnetic circuit hybrid excitation generator (PMC-HEG) that utilizes a combination of permanent magnet and electrical excitation. It features salient pole rotors and claw pole rotors, with the latter embedded with permanent magnets, sharing a common stator. The analysis of the rotor magnetic field is conducted using both the equivalent magnetic circuit method and the subdomain method. Through an examination of the generator's electromagnetic performance, key rotor parameters related to optimization objectives are identified. Finite element simulation analysis is performed on the rotor parameters, employing various optimization algorithms to enhance the salient pole and claw pole rotors, focusing on the amplitude of the induced electromotive force and the distortion rate of the induced electromotive force as optimization targets. The final optimized parameter values are obtained. A prototype is fabricated and tested, with experimental results confirming the reliability of the optimization method. The optimized parallel magnetic circuit hybrid excitation generator demonstrates an increase in the amplitude of the induced electromotive force, an improvement in the fundamental wave of the induced electromotive force, a reduction in harmonic distortion rate, and a significant enhancement in overall output performance.

Key words: hybrid excitation generator, parallel magnetic circuit, evolutionary algorithm, response surface methodology, multi-objective optimization

1. Introduction

With the continuous development of the automobile industry, the automobile intelligent and electronic upgrading, the requirements of the automobile power system are increasing, the generator as the core of the automobile power system, the output efficiency and control performance of the generator are also increasing. For the common generator, according to the excitation method, generators can be divided into permanent magnet generators, electrically excited generators, and hybrid electric excitation generators [1–3]. Among them, permanent magnet generators are simple in structure, reliable in operation, small in size and light in quality, but the generator magnetism is difficult to be adjusted, the magnetic circuit design is complicated, and the voltage stabilization is difficult to be controlled [4]. Electric excitation generators are easy to control and have a wide range of adjustable output voltage, but most of the power passed into the excitation winding is consumed due to the heat generated by the excitation winding, which is inefficient [5, 6]. The hybrid excitation generator parallel magnetic circuit, which produces a magnetic field synthesized in the air gap and is easy to regulate, is widely used in generators for automotive applications [7–9].

At present, many scholars have conducted some researches on the hybrid excitation generator and its electromagnetic characteristics and obtained certain research results. A new tangential/radial magnetic circuit parallel hybrid excitation synchronous motor is proposed by Yihao Xu [10], for which an equivalent magnetic circuit model is established and the principle of magnetization is analyzed. When the excitation winding of this motor is energized, the magnetic poles on the rotor teeth change alternately, forming a radial magnetic field structure; while the polarity of two adjacent permanent magnets is reversed, the magnetic field generated by the permanent magnets forms a tangential structure, and it has the same polarity as that of the radial magnetic field generated by the excitation current, and it is a parallel relationship in the magnetic circuit. Yu Shiyang proposed a new claw-pole hybrid excitation biconvex pole motor [11], and used a multilevel multi-objective optimization method to optimize the design of this motor structure, which improves the optimization computation accuracy, but at the same time increases the optimization solution time. The stator of this motor consists of a claw pole stator, armature winding, excitation winding and permanent magnet, the armature winding is wound on the claw pole, the excitation coil is placed between the front and rear claw poles, and the inter-pole permanent magnet is placed between the two claws. Cheng Z.M. proposed a double convex pole hybrid excitation motor [12] and measured and calculated the axial distribution of the reverse electromotive force air gap flux of this motor using the finite element method. The stator of this motor is a convex-pole structure, the armature winding is wound on top of the convex poles, the permanent magnets are mounted on the four corners of the stator, and the excitation winding is located in the middle of the two adjacent permanent magnets and is wound on the three convex poles of the stator. The motor has a magnetically conductive material between the permanent magnets and the excitation winding, which enhances the performance of the excitation winding in regulating the magnetic field, realizes the adjustability of the magnetic flux in the air gap of the motor, and at the same time ensures the high power density of the motor. Henneberger *et al.* proposed a series potential type hybrid excitation synchronous motor based on a DC motor [13], where the permanent magnets are surface mounted on the outer side of the convex rotor pole shoe and the excitation windings are wound on the convex pole body. This motor has the excitation magnetic field in series with the permanent magnet field, which improves the air gap magnetism of the motor and hence the motor has a high

power density. Tadashi Fukami proposed a new hybrid excitation motor [14], for which the magnetic saturation is the objective of the study, a mathematical model of the motor circuit is developed and analytical experiments are carried out to analyze the losses of the motor. This motor has permanent magnets placed between two convex poles with excitation windings wound on the convex poles and no permanent magnets placed. This motor has the electrical excitation flux in parallel with the permanent magnet flux in normal operating condition. E. Yıldırız proposed an axial magnetic field hybrid excitation synchronous motor [15] by taking advantage of the high torque density of axial motors, and finite element electromagnetic analysis and parameter optimization were carried out for the basic topology and different excitations of this motor. The rotor core of this motor is a convex pole rotor without magnetic potential source, and each side of the stator core has two sets of slots, one set of slots is larger to place the excitation windings and the other set of slots is smaller to place the three-phase AC windings. The excitation windings are placed in a toroidal fashion within the stator core and permanent magnets are placed in the slot openings of the excitation winding slots to help reverse the polarity of the magnetic flux when the excitation windings are energized.

Through the above analysis and comprehensive specific engineering applications, this paper proposes a new structure form of a claw-pole electromagnetic and permanent magnet parallel magnetic circuit hybrid excitation generator (PMC-HEG) for the electromagnetic characteristics of a hybrid electric excitation generator, which adopts an electric excitation claw pole rotor and the salient pole rotor coaxial parallel, sharing a stator structure, and adopts a combined structure of a V-type permanent magnet and a tile-type permanent magnet in the salient pole rotor, and provides the main source of a magnetic field in the air gap. The claw pole rotor is embedded with permanent magnets between poles to increase power density and overload capacity. The structure of the new parallel magnetic circuit generator is shown in Fig. 1.
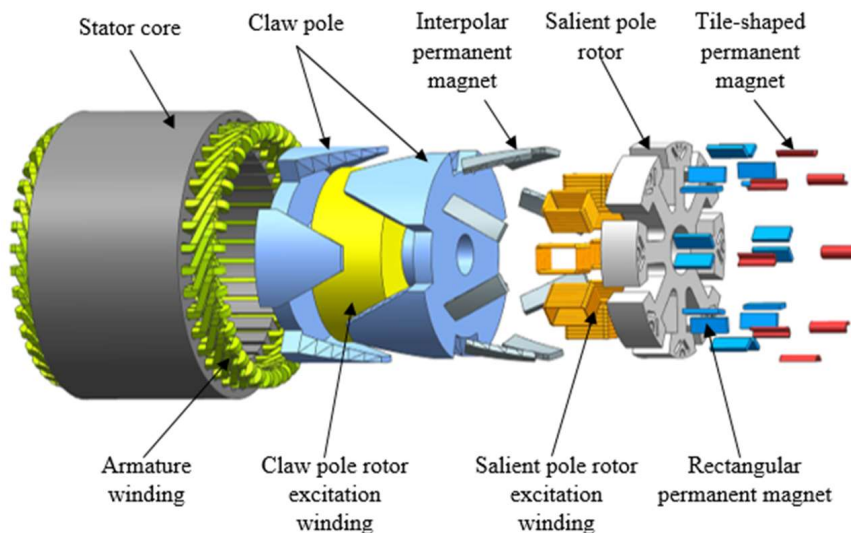

Fig. 1. Structure of PMC-HEG

Compared with the conventional claw pole electric excitation rotor, this hybrid excitation claw pole rotor inter-pole permanent magnet magnetic circuit (PMMC) and the electric excitation magnetic circuit (EEMC) of the electric excitation winding form a PMC in the radial direction. The PMMC generated by the embedded combined permanent magnet of the salient pole rotor and the EEMC of the pole body electric excitation winding are connected in series, forming a magnetic pole structure of a dual mixed-excitation rotor in which the permanent magnet of the salient pole rotor is connected in series with the EEMC in the radial direction. The permanent magnet of the hybrid electric excitation claw pole rotor is connected in parallel with the EEMC, and the magnetic circuit of the dual rotor is connected in parallel in the axial direction, so that the generator's internal space is highly utilized, and the generator has a good magnetizing capability. For the generator-induced electromotive force amplitude and distortion rate and other output performance as the optimization objective, the response surface method is used for the claw pole rotor to obtain the fitting equations of the optimized parameters, and the optimization of the fitting equations shortens the time of the traditional three-dimensional simulation optimization of the claw pole rotor. The convex pole rotor adopts the combined permanent magnet, which has better magnetizing effect and output performance, and the multi-objective joint simulation is adopted for the convex pole rotor to ensure the accuracy of the optimization results.

2. Electromagnetic performance analysis of hybrid excitation generator

2.1. Claw pole rotor equivalent magnetic circuit model

There are two sources of magnetic potential in the magnetic circuits of both the salient pole rotor and the claw pole rotor of the hybrid electric excitation generator, which are supplied by the electric excitation windings and the permanent magnets, respectively. The magnetic circuits of the two magnetic potential sources are shown in Fig. 2.

G_{e2} is the equivalent internal magnetic conductivity of the claw-pole electric excitation winding, $G_{\delta e2}$ is the additional air gap magnetic conductivity between the claw pole electric excitation winding and the claw pole rotor yoke, G_{z1} is the magnetic conductivity of the claw pole rotor yoke, G_{z2} is the magnetic conductivity of the flange of the claw pole rotor, G_{z3} is the magnetic conductivity of the claw portion of the claw pole rotor, $G_{\delta 4}$ is the air gap magnetic conductivity between the claw-pole rotor core corresponding to the electric excitation winding and the stator core, G_{δ} is the air gap magnetic conductivity between the claw-pole rotor core and the stator core corresponding to the inter-pole permanent magnets, G_{st} is the stator tooth magnetic conductivity corresponding to each pole of the claw pole rotor, G_{sy4} is the stator yoke magnetic conductivity corresponding to the electric excitation winding under a single claw pole, G_{sy5} is the stator yoke magnetic conductivity corresponding to the inter-pole permanent magnet under a single claw pole, $G_{\delta lz1}$ is the stator yoke magnetic conductivity corresponding to an inter-polar permanent magnet with a single claw pole, $G_{\delta lz2}$ is the leakage magnetic conductivity between neighboring claw poles, G_{mr} is the equivalent internal magnetic conductivity of the inter-polar permanent magnet, Φ_{e2} is the magnetic flux of the magnetic circuit of the claw pole electric excitation winding, Φ_{mr} is the flux of the magnetic circuit of the inter-pole permanent magnet, Φ_{elz1} is the flux leakage through the inter-pole permanent magnet between the front and rear claw poles in the EEMC, Φ_{elz2} is the flux leakage through the stator teeth in the EEMC, Φ_{mrl1} is the flux leakage of the front
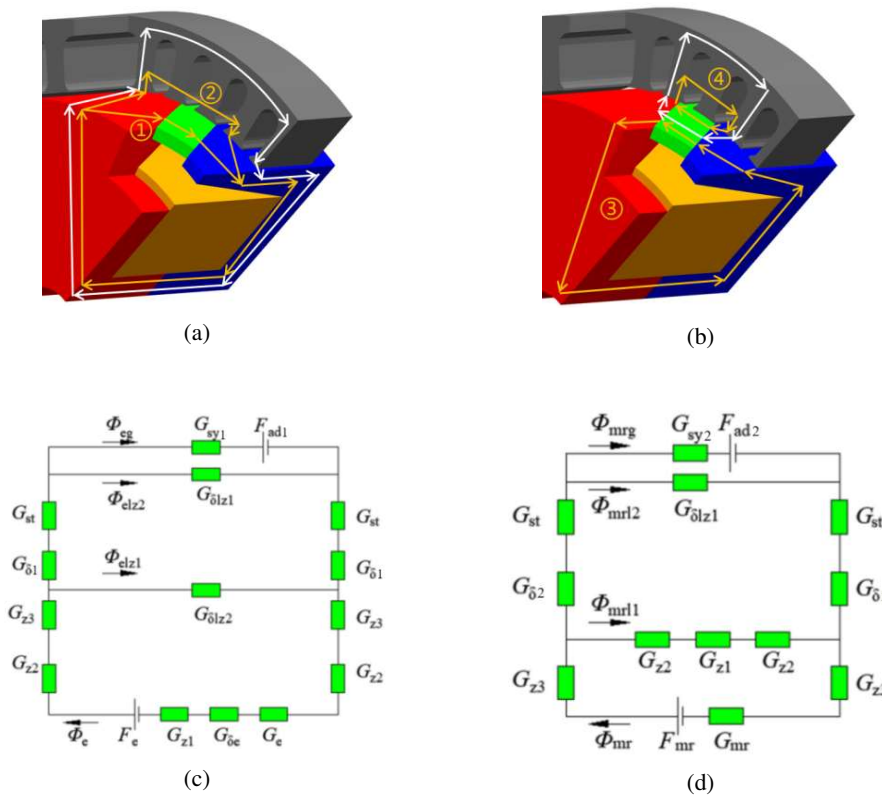
Fig. 2. Distribution diagram of the main magnetic circuit of PMC-HEG: (a) EEMC for claw pole rotor; (b) PMMC for claw pole rotor; (c) equivalent magnetic circuit diagram of claw pole rotor EEMC; (d) equivalent magnetic circuit diagram of claw-pole rotor PMMC

and rear claw poles in the PMMC, and Φ_{mrl2} is the flux leakage between the stator teeth in the PMMC. F_{e2} is the magnetic potential of the excitation source of the claw pole rotor, F_{mr} is the magnetic potential of the inter-polar permanent magnets of the claw pole rotor, F_{ad4}, F_{ad5} are the shaft straightening armature antimagnetic potentials of the EEMC and PMMC, respectively, and at no-load condition, $F_{ad4} = F_{ad5} = 0$.

Equivalent magnetic circuit models for the EEMC and PMMC are solved by Kirchhoff's law, respectively [16–18], and the following assumptions are made:

1. Neglecting armature winding end effects.

2. The permanent magnets are magnetized uniformly and the demagnetization curve varies linearly.

3. Assuming infinite stator-rotor permeability.

The magnetic flux equations for the EEMC are as follows:

$$
\begin{cases}
\Phi_e = \Phi_{elz1} + \Phi_{elz2} + \Phi_{elz1} + \Phi_{eg} \\[2mm]
F_e = \Phi_e \left(\dfrac{2}{G_{z2}} + \dfrac{2}{G_{z3}} + \dfrac{1}{G_{\delta e}} + \dfrac{1}{G_e} + \dfrac{1}{G_{z1}} \right) + \dfrac{\Phi_{elz1}}{G_{mr}} \\[2mm]
\dfrac{\Phi_{elz1}}{G_{mr}} = (\Phi_e - \Phi_{elz1}) \left(\dfrac{2}{G_{\delta l}} + \dfrac{2}{G_{st}} \right) + \dfrac{\Phi_{elz2}}{G_{\delta lz1}} \\[2mm]
F_{ad1} = \dfrac{\Phi_{eg}}{G_{sy1}} - \dfrac{\Phi_{elz2}}{G_{\delta lz1}}
\end{cases}
, \tag{1}
$$

$$
\begin{cases}
\Phi_{mr} = \Phi_{mrl1} + \Phi_{mrl2} + \Phi_{mrg} \\[2mm]
F_{mr} = \Phi_{mr} \left(\dfrac{2}{G_{z3}} + \dfrac{1}{G_{mr}} \right) + \Phi_{mrl1} \left(\dfrac{2}{G_{z2}} + \dfrac{1}{G_{z1}} \right) \\[2mm]
\Phi_{mr} = \left(\dfrac{2}{G_{z3}} + \dfrac{1}{G_{mr}} \right) = (\Phi_{mr} - \Phi_{mrl1}) \left(\dfrac{2}{G_{\delta 2}} + \dfrac{2}{G_{st}} \right) + \dfrac{\Phi_{mrl2}}{G_{\delta lz2}} \\[2mm]
F_{ad2} = \dfrac{\Phi_{mrg}}{G_{sy2}} - \dfrac{\Phi_{mrl2}}{G_{\delta lz1}}
\end{cases}
. \tag{2}
$$

2.2. The primary magnetic conductivity calculations for the claw pole rotor

1. The equivalent magnetic potential F_{e2} of the claw pole excitation winding is:

$$ F_{e2} = N_{e2} i_f, \tag{3} $$

where N_{e2} is the number of turns of the claw pole electric excitation winding and i_f is the excitation current.

2. Inter-pole permanent magnet magnetic potential F_{mr} is:

$$ F_{mr} = H_c h_{m1}, \tag{4} $$

where H_c is the coercivity force of the permanent magnet and h_{m1} is the radial thickness of the inter-pole permanent magnet.

3. Equivalent internal magnetic conductivity of the claw-pole electric excitation winding G_{e2} is:

$$ G_{e2} = \mu_0 \mu_z \frac{\pi \left(D_{ce}^2 - D_{ri}^2 \right)}{2 \left(2L_{ef} - h_{fl} \right)}, \tag{5} $$

where: u_z is the relative conductance of the claw pole material; D_{ce} is the outer diameter of the claw pole yoke; D_{ri} is the inner diameter of the claw pole rotor; L_{ef} is the claw pole axial length; and h_{fl} is the flange thickness.

4. The yoke magnetic conductivity corresponding to each pole of the claw pole G_{z1} is:

$$ G_{z1} = \mu_0 \mu_z \frac{\pi \left(D_{ce}^2 - D_{ri}^2 \right)}{4 L_{ef2}}, \tag{6} $$

5. Flange magnetic conductivity corresponding to each pole of the claw pole G_{z2} is:

$$G_{z2} = \mu_0 \mu_z \frac{h_{fl} \alpha_r \pi R_{fl}}{8 \left(R_w - \dfrac{D_{ce}}{2} \right)}, \tag{7}$$

where α_r is the claw root polar arc coefficient and R_w is the radius of the outer circle of the claw pole.

6. Magnetic conductivity of the claw pole G_{z3} is:

$$G_{z3} = \mu_0 \mu_r \frac{b_{z1} \left(h_{zj} + h_{zg} \right)}{2 L_{ef2}}, \tag{8}$$

where b_{z1} is the axial length of the claw.

7. Main air gap magnetic conductivity corresponding to each pole of the claw pole $G_{\delta 1}$ is:

$$G_{\delta 1} = \mu_0 \mu_r \frac{\pi R_w L_{ef2}}{4 p \delta_1}, \tag{9}$$

where δ_1 is the length of the main air gap between the claw pole rotor and stator teeth, $\delta_1 = 0.5$ mm.

8. Additional air gap magnetic conductivity between the electric excitation winding bracket and the claw-pole rotor yoke $G_{\delta e2}$ is:

$$G_{\delta e2} = \mu_0 \frac{\pi D_{ce} h_{ce}}{\delta_2}. \tag{10}$$

In the formulas, h_{ce} is the axial length of the claw pole rotor yoke; δ_2 is the length of the air gap between the electric excitation winding and the claw pole rotor yoke, $\delta_2 = 0.1$ mm.

2.3. Electromagnetic analysis calculation of the salient pole rotor

A finite element model of the convex rotor is established, and the magnetic field distribution of the magnetic density and magnetic lines of force of the convex rotor is obtained as shown in Fig. 3. The figure shows that in the magnetic field distribution of the finite element model of the convex rotor, the magnetic circuit of the convex rotor enters the air gap from the pole shoe, and eventually forms a complete closed flux circuit through the stator teeth, yoke, and return from the neighboring poles. The convex pole rotor has a higher magnetic field density around the permanent magnet steel, the combined permanent magnet steel has a higher polymagnetization at the air gap, and the permanent magnet steel separator bridge is saturated with leakage magnetism. Based on the magnetic field distribution in the finite element model in Fig. 3 and the structural characteristics of the convex-pole rotor, the convex-pole rotor is divided into four sub-domains as in Fig. 4 stator slot I, stator slot opening II, air gap III, and permanent magnets IV, and a mathematical model is established to further analyze the distribution of the convex-pole rotor magnetic density.

In Fig. 4, $R_1 \sim R_5$ is the radius of the corresponding boundary. b_{s0}, b_{s1} are the mechanical angles occupied by the stator slots and slots after the equivalent model, respectively. To simplify the mathematical model, the following assumptions are made:

1. Ignore eddy current effects and end effects.
2. Permanent magnet material demagnetization curve is linear.
3. The current density at the coil edge in the stator slot is uniformly distributed and has only a component in the *z*-axis direction.
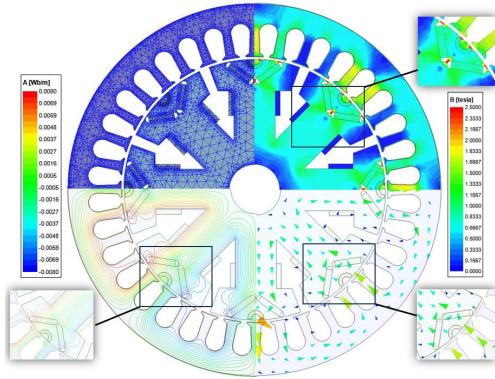4. The magnetic permeability of the stator-rotor core is infinity.

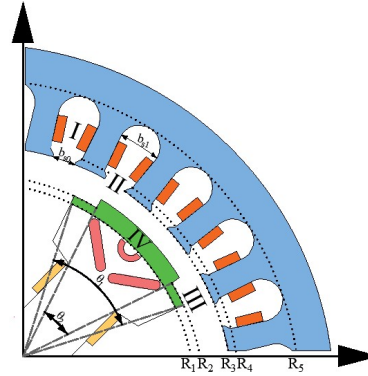Fig. 3. A Convex pole rotor finite element model magnetic field distribution

Fig. 4. Schematic diagram of subfields division of salient pole rotor

Applying Poisson's equation to the positions of the subdomains I and IV magnetic vectors, the corresponding partial differential equations are:

$$\begin{cases} \dfrac{\partial^2 A_{zIi}}{\partial r^2} + \dfrac{1}{r}\dfrac{\partial A_{zIi}}{\partial r} + \dfrac{1}{r^2}\dfrac{\partial^2 A_{zIi}}{\partial \alpha^2} = -\mu_0 J, \\ \qquad\qquad R_4 < r < R_5, \quad \alpha_i < \alpha < \alpha_i + b_{s1} \\ \dfrac{\partial^2 A_{zIVi}}{\partial r^2} + \dfrac{1}{r}\dfrac{\partial A_{zIVi}}{\partial r} + \dfrac{1}{r^2}\dfrac{\partial^2 A_{zIVi}}{\partial \alpha^2} \le -\dfrac{\mu_0}{r}\left(M_\alpha - \dfrac{\partial M_r}{\partial \alpha}\right), \\ \qquad\qquad R_1 < r < R_2, \quad \dfrac{\pi - 2\theta_1}{12} < \alpha < \dfrac{\pi + 10\theta_1}{12} \end{cases} \quad (11)$$

Based on assumption 4 above, and the continuity of the magnetic field in the neighboring subdomains, the subdomains I and IV boundary conditions are therefore:

$$\begin{cases} \left.\dfrac{\partial A_{zIi}}{\partial r}\right|_{r=R_4} = 0, \quad \left.\dfrac{\partial A_{zIi}}{\partial \alpha}\right|_{\alpha=\alpha_i} = 0, \quad \left.\dfrac{\partial A_{zIi}}{\partial \alpha}\right|_{\alpha=\alpha_i+b_{s0}} = 0, \quad \left.\dfrac{\partial A_{zIi}}{\partial r}\right|_{r=R_4} = \left.\dfrac{\partial A_{zIIi}}{\partial r}\right|_{r=R_4} \\ \left.\dfrac{\partial A_{zIVi}}{\partial \alpha}\right|_{\alpha=\frac{\pi-2\theta_1}{12}} = 0, \quad \left.\dfrac{\partial A_{zIVi}}{\partial \alpha}\right|_{\alpha=\frac{\pi+10\theta_1}{12}} = 0, \quad \left.\dfrac{\partial A_{zIVi}}{\partial r}\right|_{r=R_1} = \left.\dfrac{\partial A_{zIIIi}}{\partial r}\right|_{r=R_1} \end{cases}, \quad (12)$$

where: *l* is the number of space harmonic logarithms in the subfield of the permanent magnet; α_i is the mechanical angle occupied by the stator slots; θ_1 is the mechanical angle occupied by each pole of the salient pole rotor.

The generalized solutions for subfields I and IV were obtained by the method of separated variables:

$$
A_{zIi} = -\frac{\mu_0 (J_{i1} + J_{i2})}{8} r^2 \ln r
$$

$$
+ \sum_n \left\{ \begin{array}{l} \left[A^I \left(\frac{R_4}{R_5} \right) \left(\frac{r}{R_5} \right)^n + B^I \left(\frac{r}{R_4} \right)^n \right] \cos \left[\left(\frac{n\pi}{b_{sa}} \right) (\alpha + b_{s1} - \alpha_i) \right] \\ + \dfrac{2\mu_0 (J_{i1} + J_{i2}) \sin (n\pi/2)}{n\pi \left[\left(\dfrac{n\pi}{b_{s1}} \right)^2 - 4 \right]} \left[r^2 - \frac{2}{E_n} R_5^2 \left(\frac{r}{R_5} \right)^n \right] \cos \left[\left(\frac{n\pi}{b_{s1}} \right) (\alpha + b_{s1} - \alpha_i) \right] \end{array} \right\}, \quad (13)
$$

$$
A_{zIVi} = A^{IV} + B^{IV} \ln r + \sum_l \left[C^{IV} \left(\frac{r}{R_3} \right)^l + D^{IV} \left(\frac{r}{R_2} \right)^{-1} \right] \cos \left(\alpha + \frac{\theta_0 R_1}{2R_3} - \alpha_i \right)
$$

$$
+ \sum_l \mu_0 \left(\frac{M_{r1} - M_{\alpha 1}}{2} \ln r \right) \cos \left(\frac{l\pi}{b_{s0}} \right) \left(\alpha + \frac{\theta_0 R_1}{2R_3} - \alpha_i \right), \quad (14)
$$

where: A^I, B^I, A^{IV}, B^{IV}, C^{IV}, D^{IV} are the harmonic coefficients of the stator slot subfields; α is the circumferential angle; M_{r1}, $M_{\alpha 1}$ are the harmonic component of the tangential and radial components of the permanent magnet's remanent magnetism.

The radial and tangential components of the magnetic density of subfields I and IV are obtained:

$$
\left\{ \begin{array}{l} B_{zIr} = -\sin \left[\left(\frac{n\pi}{b_{s0}} \right) (\alpha + b_{s0} - \alpha_i) \right] \\ \times E_n \sum_n \left\{ \begin{array}{l} \left[A^I \left(\frac{R_4}{R_5} \right) \left(\frac{r}{R_5} \right)^n + B^I \left(\frac{r}{R_4} \right)^n \right] \\ -\mu_0 \dfrac{n\pi}{b_{s0}r} \dfrac{2 (J_{i1} + J_{i2}) \sin \left(\frac{n\pi}{2} \right)}{n\pi \left[\left(\dfrac{n\pi}{b_{s0}} \right)^2 - 4 \right]} \left[r^2 - \frac{2}{E_n} R_5^2 \left(\frac{r}{R_4} \right)^n \right] \end{array} \right\} \\ B_{It} = -\sum_n \left\{ \begin{array}{l} n \left[A^I \left(\frac{R_4}{R_5} \right) \left(\frac{r}{R_5} \right)^{n-1} + B^I \left(\frac{r}{R_4} \right)^{n-1} \right] \cos \left[E_n (\alpha + b_{s0} - \alpha_i) \right] \\ -\mu_0 \dfrac{2 (J_{i1} + J_{i2}) \sin (n\pi/2)}{n\pi \left[\left(\dfrac{n\pi}{b_{s0}} \right)^2 - 4 \right]} \left[2r - \frac{2}{E_n} n R_5^2 \left(\frac{r}{R_4} \right)^{n-1} \right] \\ + \cos \left[\left(\frac{n\pi}{b_{s0}} \right) (\alpha + b_{s0} - \alpha_i) \right] \frac{\mu_0}{2} J_{i0} r \ln r + \frac{\mu_0}{4} J_{i0} r \end{array} \right\} \end{array} \right., \quad (15)
$$

$$
\begin{cases}
B_{\mathrm{IVr}} = -\dfrac{1}{r} \sum_l \left[C^{\mathrm{IV}} \left(\dfrac{r}{R_2} \right)^l + D^{\mathrm{IV}} \left(\dfrac{r}{R_1} \right)^{-l} \right] \sin\left(\alpha + \dfrac{\theta_2 R_1}{2R_2} - \alpha_i \right) \\[4mm]
\qquad\qquad - \dfrac{1}{r} \dfrac{l\pi}{b_{\mathrm{s0}}} \sum_l \mu_0 \left(\dfrac{M_{\mathrm{rl}} - M_{\alpha l}}{2} \ln r \right) \sin\left(\dfrac{l\pi}{b_{\mathrm{s0}}} \right) \left(\alpha + \dfrac{\theta_2 R_1}{2R_2} - \alpha_i \right) \\[4mm]
B_{\mathrm{IVt}} = -\dfrac{B^{\mathrm{IV}}}{r} - \sum_l \left[l C^{\mathrm{IV}} \left(\dfrac{r}{R_2} \right)^{l-1} - l D^{\mathrm{IV}} \left(\dfrac{r}{R_1} \right)^{-l-1} \right] \cos\left(\alpha + \dfrac{\theta_2 R_1}{2R_2} - \alpha_i \right) \\[4mm]
\qquad\qquad - \sum_l \mu_0 \left(\dfrac{M_{\mathrm{rl}} - M_{\alpha l}}{2r} \right) \cos\left(\dfrac{l\pi}{b_{\mathrm{s0}}} \right) \left(\alpha + \dfrac{\theta_2 R_1}{2R_2} - \alpha_i \right)
\end{cases} . \tag{16}
$$

Similarly, the Laplace partial differential equations are established for the stator slot opening domain II and air gap domain III, and the following boundary conditions are established using the magnetic field continuity in the neighboring subdomains.

$$
\begin{cases}
\dfrac{\partial^2 A_{\mathrm{zII}i}}{\partial r^2} + \dfrac{1}{r} \dfrac{\partial A_{\mathrm{zII}i}}{\partial r} + \dfrac{1}{r^2} \dfrac{\partial^2 A_{\mathrm{zII}i}}{\partial \alpha^2} = 0, \\[3mm]
\qquad R_3 < r < R_4, \quad \alpha_i + \dfrac{b_{\mathrm{s1}} - b_{\mathrm{s0}}}{2} < \alpha_{\mathrm{t}} < \alpha_i + \dfrac{b_{\mathrm{s1}} + b_{\mathrm{s0}}}{2} \\[3mm]
\dfrac{\partial^2 A_{\mathrm{zIII}i}}{\partial r^2} + \dfrac{1}{r} \dfrac{\partial A_{\mathrm{zIII}i}}{\partial r} + \dfrac{1}{r^2} \dfrac{\partial^2 A_{\mathrm{zIII}i}}{\partial \alpha^2} = 0, \\[3mm]
\qquad R_2 < r < R_3, 0 < \alpha < \dfrac{\pi}{6}
\end{cases} , \tag{17}
$$

$$
\begin{cases}
\left. \dfrac{\partial A_{\mathrm{zII}i}}{\partial \alpha} \right|_{\alpha = \alpha_i + \frac{b_{\mathrm{s1}} - b_{\mathrm{s0}}}{2}} = 0, \qquad\qquad \left. \dfrac{\partial A_{\mathrm{zII}i}}{\partial \alpha} \right|_{\alpha = \alpha_i + \frac{b_{\mathrm{s1}} + b_{\mathrm{s0}}}{2}} = 0, \\[5mm]
\left. \dfrac{\partial A_{\mathrm{zII}i}}{\partial r} \right|_{r = R_3} = \left. \dfrac{\partial A_{\mathrm{zII}i}}{\partial r} \right|_{r = R_3}, \qquad \left. \dfrac{\partial A_{\mathrm{zII}i}}{\partial r} \right|_{r = R_4} = \left. \dfrac{\partial A_{\mathrm{zII}i}}{\partial r} \right|_{r = R_4} \\[5mm]
\left. \dfrac{\partial A_{\mathrm{zII}i}}{\partial r} \right|_{r = R_2} = \left. \dfrac{\partial A_{\mathrm{zIV}i}}{\partial \alpha} \right|_{r = R_2}, \\[5mm]
\left. \dfrac{\partial A_{\mathrm{zII}i}}{\partial r} \right|_{r = R_3} = \begin{cases} \left. \dfrac{\partial A_{\mathrm{zII}i}}{\partial \alpha} \right|_{r = R_3}, & \alpha_i + \dfrac{b_{\mathrm{s1}} - b_{\mathrm{s0}}}{2} < \alpha < \alpha_i + \dfrac{b_{\mathrm{s1}} + b_{\mathrm{s0}}}{2} \\[4mm] \left(1 - \dfrac{\mu_1 \delta}{\mu_0 h_{\mathrm{m3}}} \right) \left. \dfrac{\partial A_4}{\partial \alpha} \right|_{r = R_2} \end{cases}
\end{cases} \tag{18}
$$

The radial and tangential components of the subdomain I and IV magnetic densities are obtained:

$$
\begin{cases}
B_{\mathrm{IIr}} = -\dfrac{m}{r} \sum_m \left\{ \left[A^{\mathrm{II}} \left(\dfrac{r}{R_4} \right)^m + B^{\mathrm{II}} \left(\dfrac{r}{R_3} \right)^{-m} \right] \sin\left[m\left(\alpha + b_{s0} - \alpha_i \right) \right] \right. \\
\qquad\qquad \left. -\dfrac{m}{r} \left[C^{\mathrm{II}} \left(\dfrac{r}{R_4} \right)^m - D^{\mathrm{II}} \left(\dfrac{r}{R_3} \right)^{-m} \right] \cos\left[m\left(\alpha + b_{s0} - \alpha_i \right) \right] \right\} \\[4mm]
B_{\mathrm{IIt}} = -\sum_m \left\{ m \left[A^{\mathrm{II}} \left(\dfrac{r}{R_4} \right)^{m-1} - B^{\mathrm{II}} \left(\dfrac{r}{R_3} \right)^{-m-1} \right] \cos\left[m\left(\alpha + b_{s0} - \alpha_i \right) \right] \right. \\
\qquad\qquad \left. - m \left[C^{\mathrm{II}} \left(\dfrac{r}{R_4} \right)^{m-1} + D^{\mathrm{II}} \left(\dfrac{r}{R_3} \right)^{-m-1} \right] \sin\left[m\left(\alpha + b_{s0} - \alpha_i \right) \right] \right\} \\[4mm]
B_{\mathrm{IIIr}} = -\dfrac{k}{r} \sum_k \left[A^{\mathrm{III}} \left(\dfrac{r}{R_3} \right)^k + B^{\mathrm{III}} \left(\dfrac{r}{R_2} \right)^{-k} \right] \sin(k\alpha) \\
\qquad\qquad +\dfrac{k}{r} \sum_k \left[C^{\mathrm{III}} \left(\dfrac{r}{R_3} \right)^k + D^{\mathrm{III}} \left(\dfrac{r}{R_2} \right)^{-k} \right] \cos(k\alpha) \\[4mm]
B_{\mathrm{IIIt}} = -\sum_k \left[k A^{\mathrm{III}} \left(\dfrac{r}{R_3} \right)^{k-1} - k B^{\mathrm{III}} \left(\dfrac{r}{R_2} \right)^{-k-1} \right] \cos(k\alpha) \\
\qquad\qquad -\sum_k \left[k C^{\mathrm{III}} \left(\dfrac{r}{R_3} \right)^{k-1} - k D^{\mathrm{III}} \left(\dfrac{r}{R_2} \right)^{-k-1} \right] \sin(k\alpha)
\end{cases}
. \quad (19)
$$

According to different subfield formulas, the air gap magnetic density distribution of the salient pole rotor can be obtained, and under the premise of neglecting the influence of the adjacent slot of the stator, the amplitude of the air gap magnetic density fundamental wave calculated by the subfield method is 0.873 T, and that obtained by the finite element method is 0.862 T, these values are similar to each other.

3. Multi-objective optimization of a parallel magnetic circuit with dual rotors

Based on the aforementioned simulation analysis, a comprehensive examination of various structural parameters of both the salient pole rotor and the claw pole rotor is conducted. The optimization objectives are the induced electromotive force amplitude and waveform distortion rate. While ensuring that all optimization parameters remain within specified constraints, different optimization algorithms are applied to each rotor. This study aims to explore the optimal solutions for the structural parameters of the dual-rotor configuration with parallel magnetic circuits under

multiple parameters and objectives. The optimization targets are to maximize the amplitude of the no-load induced electromotive force and to minimize the waveform distortion rate, represented by the following mathematical model:

$$\begin{cases} \text{Maximum}: \; f(X) = \left(\dfrac{1}{\text{THD}_U}, U_{\max} \right) \\ X = (\theta_1, b_{v1}, h_{v1}, b_z) \end{cases} . \tag{20}$$

In the formulas, $U_{\max}$ refers to the amplitude of the no-load induced electromotive force and THD_U refers to the distortion rate of the no-load induced electromotive force waveform.

3.1. Multi-objective optimization of the salient pole rotors using finite element methods and evolutionary algorithms

The angle θ_1 of the V-type permanent magnet in the salient pole rotor, along with the width b_z of the salient pole rotor, significantly influences the amplitude of the no-load induced electromotive force and the distortion rate of its waveform. In contrast, the polar arc coefficient α_s of the salient pole rotor has a relatively minor effect on the amplitude of the no-load induced electromotive force. Therefore, the polar arc coefficient is set to 0.7 to enhance the critical parameters that affect the magnetic field strength, the induced electromotive force amplitude and waveform: the tangential length b_{v1} and the magnetization thickness h_{v1} of the V-type permanent magnet. The initial values and constraints for the four optimization parameters are detailed in Table 1.

Table 1. The constraints related to the optimization parameters and objectives

Optimize parameters	Initial value	Constraints
θ_1	105°	$95° \leq \theta_1 \leq 115°$
b_{v1}	10 mm	$9 \text{ mm} \leq b_{v1} \leq 11 \text{ mm}$
h_{v1}	2.5 mm	$2 \text{ mm} \leq h_{v1} \leq 3 \text{ mm}$
b_z	16 mm	$13 \text{ mm} \leq b_z \leq 17 \text{ mm}$

Multi-objective joint simulation is carried out for the optimization parameters in the above table, and the genetic algorithm optimization scheme with the fastest computational speed is selected by system adaption. Utilizing evolutionary algorithms, a total of 100 random points were selected to determine the optimal objective values. The distribution graph of the optimization results' Pareto front is illustrated in Fig. 5.

3.2. Experimental design of response surface methodology for claw pole rotor parameters

In the optimization process of the hybrid excitation claw pole rotor, the sensitivity of the primary parameters is first calculated. This allows for an effective analysis and evaluation of the optimization objectives. By selecting parameters with high sensitivity for multi-objective and multi-parameter optimization, it is possible to significantly reduce computational losses and enhance optimization efficiency [19].
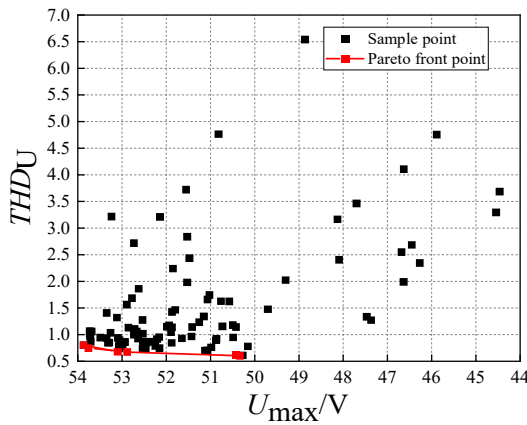
Fig. 5. Pareto frontier distribution chart

The selection of initial optimization parameters includes the thickness of the flange, the root polar arc coefficient of the claw, the thickness of the claw root, the tip polar arc coefficient of the claw, the thickness of the claw tip, and the axial length and radial thickness of the inter-pole permanent magnets in the air gap. The optimization objectives are the amplitude and waveform distortion rate of the generator's no-load induced electromotive force. The initial values for the optimization parameters are derived from the optimal values obtained in the previous section, with the specific initial values and constraints for each parameter detailed in Table 2.

Table 2. The initial values and constraints for each optimization parameter

Optimize parameters	Initial value	Constraints
h_f	8 mm	7 mm $\leq h_f \leq$ 9 mm
α_r	1.1	0.9 $\leq \alpha_r \leq$ 1.2
h_{zg}	8.5 mm	7.5 mm $\leq h_{zg} \leq$ 9 mm
α_t	0.45	0.4 $\leq \alpha_t \leq$ 0.6
h_{zj}	2.5 mm	2 mm $\leq h_{zj} \leq$ 4 mm
b_{m1}	36 mm	32 mm $\leq b_{m1} \leq$ 36 mm
h_{m1}	4 mm	3 mm $\leq h_{m1} \leq$ 5 mm

The sensitivity $S(x, y)$ of the optimization objective y with respect to the parameter x is defined as [20]:

$$\begin{cases} S(x, y) = \dfrac{\text{cov}(x, y)}{\sigma_x \sigma_y} \\ \text{cov}(x, y) = \dfrac{\sum_{i=1}^{N} (x_i - x_{avg})(y_i - y_{avg})}{N_1} \end{cases}. \tag{21}$$

In the formulas, $\text{cov}(x, y)$ is covariance; x_{avg} represents the average value of the optimization parameter x; σ_y represents the standard deviation of the optimization parameter x; y_{avg} represents

the average value of the optimization objective y; σ_y represents the standard deviation of the optimization objective y; and N_1 represents the sample space of the experimental design.

The results of the sensitivity analysis regarding the influence of all optimization parameters on the amplitude of the induced electromotive force and the waveform distortion rate are illustrated in Fig. 6.
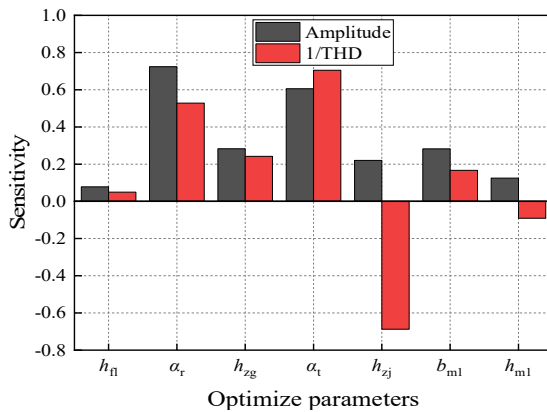

Fig. 6. An analysis of the sensitivity of the optimization objective to the optimization parameters

A higher sensitivity indicates a stronger relationship between the optimization parameters and the optimization objectives. A positive value signifies that the optimization objective increases with the rise of the optimization parameters, while a negative value indicates a decrease in the objective as the parameters increase [21]. As illustrated in Fig. 6, the impact of various optimization parameters on different optimization objectives varies. Notably, the claw root polar arc coefficient α_r, the claw tip polar arc coefficient α_t, and the claw tip thickness h_{zj} exhibit the highest sensitivity values concerning the optimization objectives. Therefore, further optimization of these three parameters is warranted, while the other parameters will retain the optimization results from the previous section.

3.3. The high sensitivity parameters of the claw pole rotor are subject to multi-objective re-optimization

Traditional multi-objective optimization methods typically rely on a single objective function for optimization, often overlooking the interactions and trade-offs between objectives. This oversight can result in algorithms failing to converge to the true Pareto front when seeking a global optimum, leading to significant consumption of computational resources and time during the optimization process. By employing response surface methodology to develop surrogate models and utilizing genetic algorithms to solve these models [22], multi-objective optimization can be effectively transformed into a single-objective optimization problem through weighted design, thereby enhancing optimization efficiency.

Conduct a response surface experimental design using the three highly-sensitive parameters mentioned above, a variance analysis is conducted on the response surface results, leading to the development of the surrogate model represented by the quadratic polynomial regression equation as shown in Eq. (22). The results of the variance analysis for the regression model are presented in Table 3.

$$
\begin{cases}
U_{\max} = -59.11469 + 145.34291\alpha_r + 101.65670\alpha_t + 0.663285h_{zj} - 23.44571\alpha_r\alpha_t \\
\qquad + \ 0.525448\alpha_r h_{zj} + 1.96077\alpha_t h_{zj} - 61.56864\alpha_r^2 - 91.75466\alpha_t^2 - 0.329559h_{zj}^2 \\
\mathrm{THD}_U = -9.28418 + 46.94447\alpha_r - 26.11956\alpha_t + 1.33904h_{zj} + 0.5441731\alpha_r\alpha_t \\
\qquad - 0.108121\alpha_r h_{zj} - 0.222972\alpha_t h_{zj} - 19.14566\alpha_r^2 + 30.41400\alpha_t^2 - 0.055029h_{zj}^2
\end{cases}
. \quad (22)
$$

Table 3. Analysis of variance in regression models

Target parameters	P-value	P-value of the null hypothesis	R^2
$U_{\max}$	0.0035	0.4051	0.9248
THD_U	< 0.0001	0.7921	0.9748

The data presented in Table 3 indicates that the P-values for both models are less than 0.01, signifying a highly significant model. The P-values for the lack of fit are 0.4051 and 0.7921, both exceeding 0.05, which suggests a high degree of model fit. The coefficients of determination R^2 are 0.9248 and 0.9748, indicating a strong correlation between the actual and predicted values. Consequently, this model effectively illustrates the relationship between the optimized parameters and the optimization objectives, demonstrating sufficient fitting accuracy to support the multi-objective genetic optimization design of the claw pole rotor based on this surrogate model.

The response surface plot illustrating the interaction effects among the three factors on $U_{\max}$ and THD_U is presented in Fig. 7.
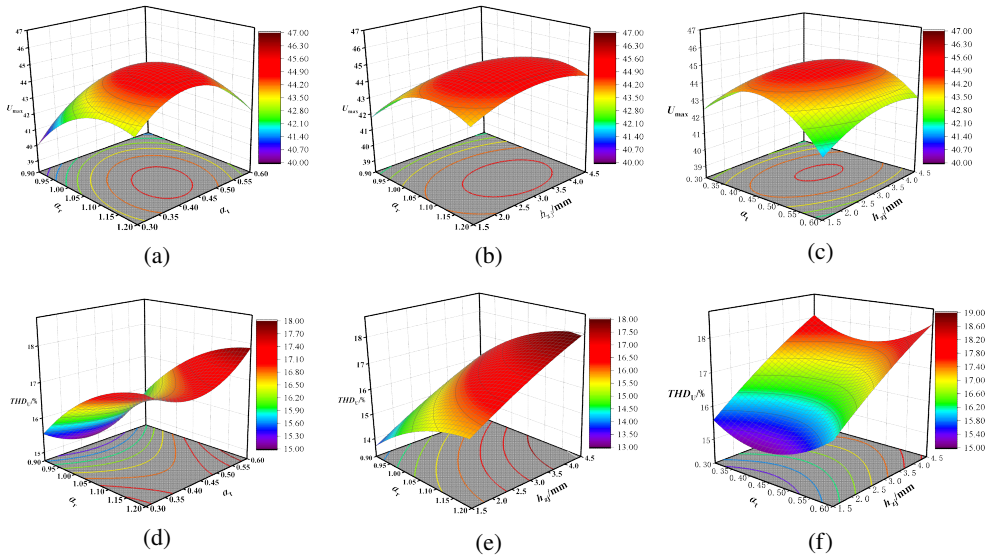

Fig. 7. The response surface plot illustrating the interactions: (a) α_r, α_t and $U_{\max}$; (b) α_r, h_{zj} and $U_{\max}$; (c) α_t, h_{zj} and $U_{\max}$; (d) α_r, α_t and THD_U; (e) α_r, h_{zj} and THD_U; (f) α_t, h_{zj} and THD_U

The analysis of Fig. 7 reveals that the influences of α_r, α_t and h_{zj} on U_{max} and THD_U exhibit varying trends and degrees of strength. Furthermore, there exists a coupling effect among the three factors, which interact with one another to collectively determine the optimal distribution for U_{max} and THD_U.

The surrogate model was imported into Workbench, and a genetic algorithm was employed to solve 100 sets of values [23, 24]. The distribution of the Pareto front for the optimization results is illustrated in Fig. 8.
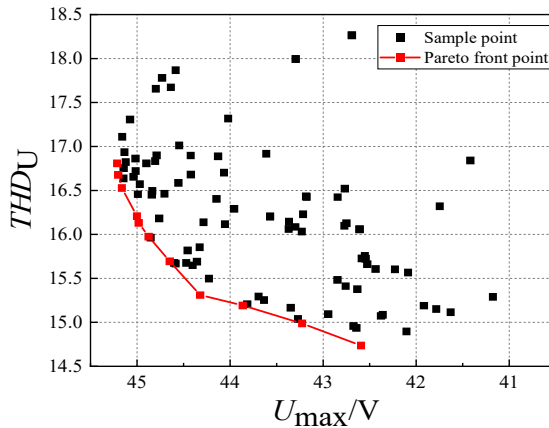
Fig. 8. Pareto frontier distribution chart

3.4. The pursuit of the optimal solution for parameter optimization

The induced electromotive force amplitude and waveform distortion rate are both evaluation criteria for the generator. During the optimization process, it is often the case that achieving an optimal solution for both parameters simultaneously is not feasible. Therefore, it is possible to assign different weights to each criterion and then subtract one from the other, thereby transforming the multi-objective optimization problem into a single-objective optimization problem [25], weighted evaluation metrics K_i:

$$\begin{cases} K_i = w_1 \dfrac{U_{max\,i}}{U_{max\,m}} - w_2 \dfrac{THD_{Ui}}{THD_{Um}} \\ w_1 + w_2 = 1 \end{cases}, \tag{23}$$

where w_1 is the weighting coefficient of the amplitude of the induced electromotive force, set $w_1 = 0.8$ and w_2 is the weighted coefficient for the induced electromotive force waveform distortion rate, set $w_2 = 0.8$. The value of U_{max} in the experiment designated as i is represented by $U_{max\,i}$ and $U_{max\,m}$ is the maximum value of all U_{max} located on the Pareto frontier. The value of THD_U in the experiment designated as i is represented by THD_{Ui} and THD_{Um} is the maximum value of all THD_U located on the Pareto frontier.

The Pareto front points calculated for the dual rotor were substituted into Eq. (23). The results indicate that the weighted evaluation metric for sample point 86 of the salient pole rotor is maximized, yielding a fundamental wave amplitude of the induced electromotive force of 43.0985 V and a waveform distortion rate of 15.6777%. Conversely, for sample point 52 of the

claw pole rotor, the weighted evaluation metric is also maximized, resulting in a fundamental wave amplitude of 44.9829 V and a waveform distortion rate of 16.1314%. The optimization outcomes are presented in Table 4.

Table 4. Optimal results

Optimize parameters	Initial value	Optimization value	Final value
$\theta_1/°$	105°	107.7	107.7
$b_{v1}/$ mm	10	10.5094	10.5
$h_{v1}/$ mm	2.5	2.4602	2.46
$b_z/$ mm	16	16.4538	16.45
α_r	1.05	1.0679	1.07
α_t	0.45	0.4492	0.45
$h_{zj}/$ mm	2.5	2.4859	2.5

Taking into account the processing precision, the final values for the V-type permanent magnet angle, the tangential length of the permanent magnet, the thickness of the magnetization, the width of the pole body, the arc coefficient at the root of the claw (α_r), the arc coefficient at the tip of the claw (α_t), and the thickness at the claw tip (h_{zj}) are determined to be 107.7°, 10.5 mm, 2.46 mm, 16.45 mm, 1.07, 0.45, and 2.5 mm, respectively.

The simulation results of the PMC-HEG are illustrated in Fig. 9.

The comparative analysis of the optimized parallel magnetic circuit generator's no-load induced electromotive force is illustrated in Fig. 9. At the rated speed, the amplitude of the
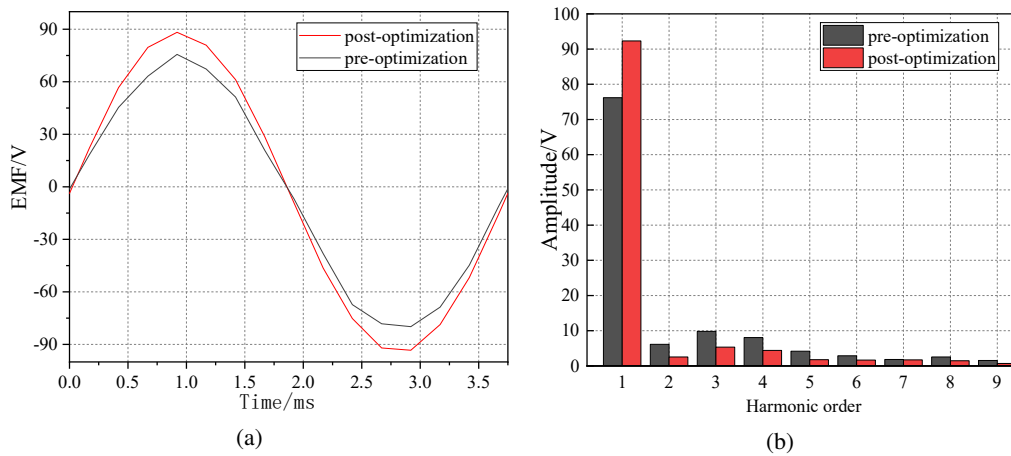
Fig. 9. The influence patterns of no-load induced electromotive force before and after optimization: (a) induced electromotive force waveform; (b) induced electromotive force amplitude

generator's no-load induced electromotive force increased from 75.59 V to 88.21 V, representing a 14.3% enhancement. Additionally, the fundamental amplitude of the induced electromotive force exhibited a significant rise from 42.1 V to 51.9 V, marking an improvement of 17.45%. Notably, the optimized third and fourth harmonics are significantly reduced, and the fifth and sixth harmonics are also reduced. The optimized induced electromotive force waveform presents better sinusoidal characteristics, which improves the voltage output efficiency of the generator and the generator power density, the distortion rate of the generator induced electromotive force waveform is lower, the generator output voltage is smoother, which is conducive to the reduction of the generator-related electromagnetic noise.

4. Performance testing of PMC-HEG

A prototype of a PMC-HEG was developed based on the optimized parameter results. An experimental platform was established to conduct tests on the prototype, with the physical representation of the entire assembly illustrated in Fig. 10. The details of the prototype are shown in Table 5.

(a)   (b)

(c)   (d)
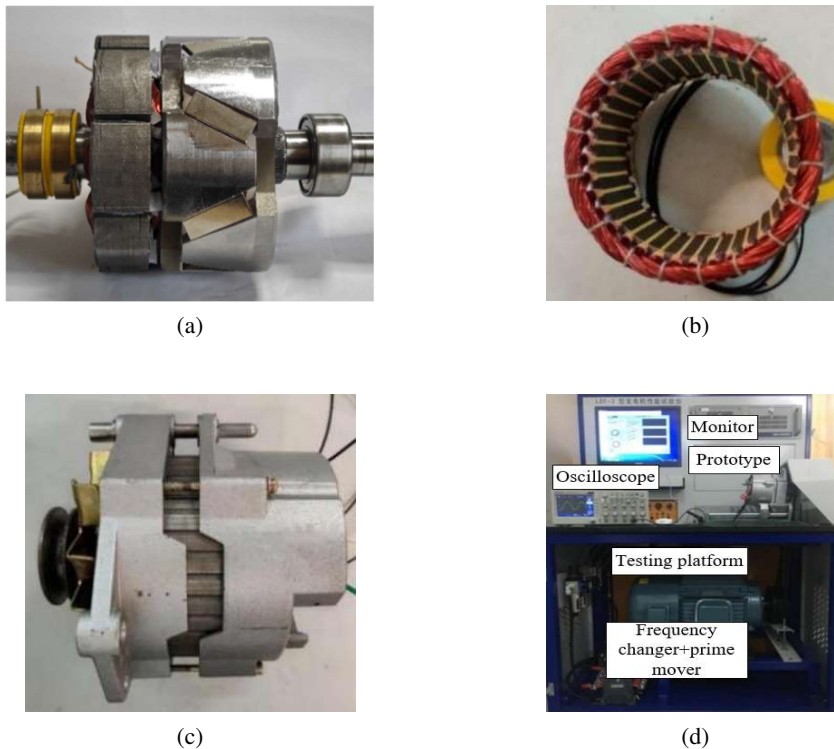
Fig. 10. Prototype and platform for experimentation: (a) rotor; (b) stator and armature windings; (c) complete assembly; (d) experimental platform

Table 5. Detailed parameters of the test prototype

Technical indicators	Value	Technical indicators	Value
Rated voltage/V	28	Rated power/W	1000
Rated speed/rpm	4000	Polar logarithm	4
Number of stator slots	36	Phase number	3
Insulation class	E	Protection class	IPX4
Output method	DC	Operating temperature/°	–40~75

1) Testing of the no-load characteristics of the generator

The rotational speed of the PMC-HEG was established at a rated speed of 4000 r/min, with the load set to its maximum value to simulate the no-load condition. The induced electromotive force of the generator was tested at an excitation current of 1 A, along with the direct current output voltage ranging from –3 A to 3 A. The results are illustrated in Fig. 11.
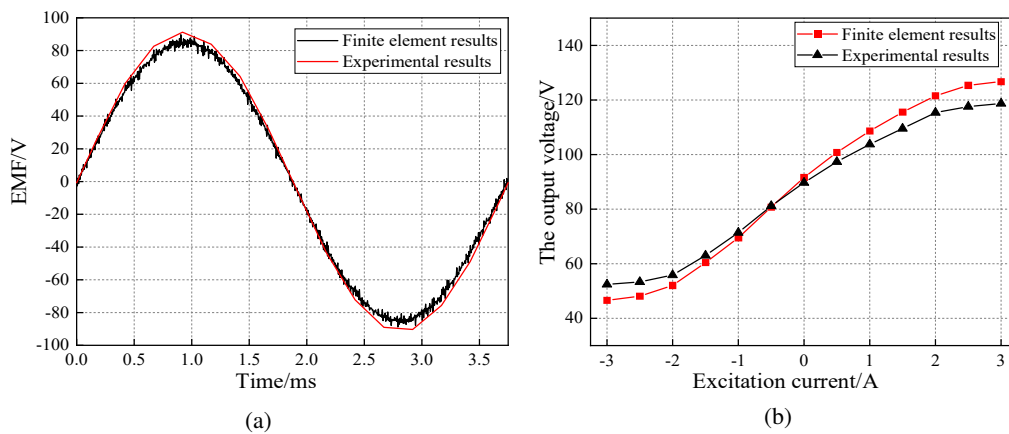
Fig. 11. The no-load characteristic curve of PMC-HEG: (a) induced electromotive force waveform diagram when the excitation current is set at 1 A; (b) the direct current output voltage

The results of the generator tests, as illustrated in Fig. 11, closely align with those obtained from finite element simulations. The experimental value for the no-load induced electromotive force was recorded at 88.7 V, while the finite element simulation yielded a value of 90.3 V, resulting in a discrepancy of 1.8%. The experimental data for the no-load characteristic curve indicates that as the excitation current increases, the output voltage of the generator correspondingly rises. Notably, within the range of excitation current from –2 A to 2 A, the output voltage of the generator exhibits significant variation. However, when the excitation current exceeds 2 A or falls below –2 A, the rate of change in output voltage diminishes. The experimental findings suggest that adjusting the magnitude and direction of the excitation current can effectively modulate the no-load output voltage, allowing it to vary within a broad range from 52.4 V to 118.7 V.

2) Testing of the generator speed and load variations

The generator was subjected to a constant-speed variable load test at a rated speed of 4000 r/min with an excitation current of 2 A, while a variable pure resistive load was connected to the direct current side. Additionally, a constant-load variable speed test was conducted with the generator loaded to a rated resistance of 0.784 Ω, where the speed was incrementally increased from 1500 r/min to 4500 r/min. During this process, the excitation current was adjusted to maintain a stable output voltage of 28 V on the direct current side of the generator. The output voltage of the generator was measured under various load conditions, and the excitation current was recorded at different speeds. The curves for the variable speed and load, constant speed and load, and constant load and variable speed of the generator are presented in Table 6 and Figs. 12 and 13.

Table 6. Results of variable speed and load testing for PMC-HEG

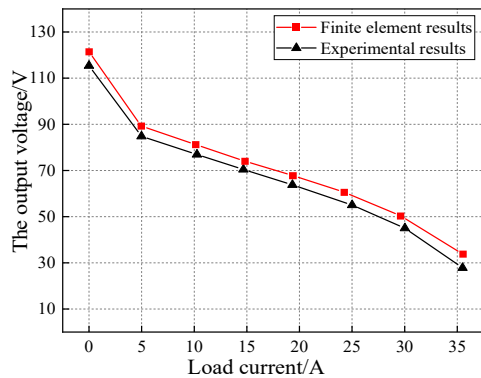| Prototype number	2000 r/min			4000 r/min			4500 r/min		
	980 W	1000 W	1020 W	980 W	1000 W	1020 W	980 W	1000 W	1020 W
1	27.9 V	28.1 V	27.8 V	28.1 V	28.2 V	28.1 V	28.2 V	28.3 V	28.1 V

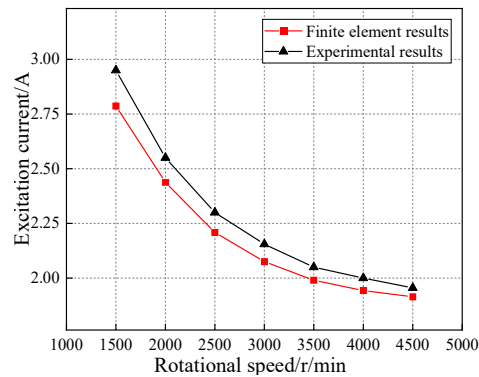Fig. 12. The constant speed variable load curve of PMC-HEG

Fig. 13. The constant load speed curve of PMC-HEG

The analysis of Table 6, Fig. 12, and Fig. 13 reveals that as the generator speed increases from 2000 r/min to 4500 r/min, the load power rises from 980 W to 1020 W, while the output voltage on the direct current side of the generator remains consistently stable at 28 V, with a maximum deviation of only 0.3 V. This indicates the generator's capability to maintain an output voltage close to the rated voltage under varying speed and load conditions. When the generator operates at a constant speed with changing loads, an increase in the direct current side load results in a corresponding rise in load current, which subsequently leads to a decrease in the output voltage. Specifically, when the excitation current is set at 2 A and the load current reaches a rated value of 35.7 A, the output voltage on the direct current side measures 27.81 V. If the load exceeds the rated capacity, the generator requires a higher excitation current to ensure that the output

voltage meets a rated level of 28 V. Furthermore, when the load remains constant and the output voltage is maintained at 28 V, an increase in the generator speed from 1500 r/min to 4500 r/min is accompanied by a gradual reduction in excitation current, with the rate of change diminishing over time. At a speed of 1500 r/min, the excitation current is recorded at 2.95 A, indicating that the magnetic circuit within the core is nearing saturation. The finite element analysis results are slightly lower than the experimental findings, and as the excitation current decreases, the discrepancy between the two results progressively narrows.

5. Conclusions

This paper presents a structure for a parallel magnetic circuit generator that features a hybrid excitation salient pole rotor and claw pole rotor, both equipped with permanent magnets. The analysis of the magnetic circuit and magnetic field for the claw pole and salient pole rotors is conducted using the equivalent magnetic circuit method and the subdomain method, respectively. Mathematical models are established for the magnetic flux equations of the claw pole rotor and the magnetic flux density components of the salient pole rotor across different subdomains. To enhance the amplitude of the no-load induced electromotive force and reduce the harmonic distortion rate of the induced electromotive force, evolutionary algorithms and response surface fitting methods are employed to optimize the structural parameters of the salient pole and claw pole rotors, which influence the generator's induced electromotive force amplitude and waveform. Based on the optimized parameters, a prototype is constructed, and experimental results indicate that under rated speed and excitation current adjustments ranging from –3 A to 3 A, the output voltage varies within a broad range of 52.4 V to 118.7 V, showing minimal deviation from the optimized simulation results. Under the variable speed and variable load experiments, the output voltage of the generator DC side is always stabilized near 28 V, which has a good voltage stabilization performance. In this paper, the generator-induced electromotive force amplitude and distortion rate for the optimization objective are used to obtain a good voltage output capability. The subsequent generator losses can be further studied to improve the generator output efficiency and to ensure that the generator operates at a reasonable operating temperature.

References

[1] Rouholla R., Ehsan S.A., Asghar S.G., *Design of a high speed interior claw synchronous reluctance machine*, International Transactions on Electrical Energy Systems, vol. 31, no. 12 (2021), DOI: 10.1002/2050-7038.13200.

[2] Bailey G., Mancheri N., Acker V.K., *Sustainability of Permanent Rare Earth Magnet Motors in (H)EV Industry*, Journal of Sustainable Metallurgy, vol. 3, no. 3, pp. 611–626 (2017), DOI: 10.1007/s40831-017-0118-4.

[3] Rigatos G., Abbaszadeh M., Siano P., *A nonlinear optimal control approach for permanent magnet AC motors with non-sinusoidal back EMF*, Electrical Engineering, vol. 104, no. 4, pp. 1–26 (2022), DOI: 10.1007/S00202-021-01475-3.

[4] Wrobel R., *Thermal Management of Electrical Machines for Propulsion - Challenges and Future Trends*, Archives of Electrical Engineering, vol. 71, no. 1, pp. 175–187 (2022), DOI: 10.24425/aee.2022.140204.

[5] Zhao J., Lin M., Fu X., *A Review and Recent Advances in Hybrid Excitation Synchronous Motors and Their Control Technologies*, Proceedings of the Chinese Society of Electrical Engineering (in Chinese), vol. 34, no. 33, pp. 1672–1695 (2014), DOI: 10.13334/j.0258-8013.pcsee.2014.33.010.

[6] Zhang Z., Wang D., Hua W., *Design, and Operation Control Technologies of Hybrid Excitation Motors*, Proceedings of the Chinese Society of Electrical Engineering (in Chinese), vol. 40, no. 24, pp. 7834–7850+8221 (2020), DOI: 10.13334/j.0258-8013.pcsee.201689.

[7] Yang C.X., Wang K., Liu Z.Y., *Research on Magnetic Regulation Characteristics of Axial-radial Flux Type Permanent Magnet Synchronous Machine*, Archives of Electrical Engineering, vol. 71, no. 1, pp. 75–90 (2022), DOI: 10.24425/aee.2022.140198.

[8] Paplicki P., *A Novel Rotor Design for a Hybrid Excited Synchronous Machine*, Archives of Electrical Engineering, vol. 66, no. 1, pp. 29–40 (2017), DOI: 10.1515/aee-2017-0003.

[9] Zhao Y., Huang W.J., Jiang W., *Optimal Design and Performance Analysis of Dual-Stator Permanent Magnet Fault-Tolerant Machine*, IEEE Transactions on Magnetics, vol. 57, no. 2, pp. 1–6 (2021), DOI: 10.1109/TMAG.2020.3026327.

[10] Xu Y., Zhu X., Liu C., *A New Type of Tangential/Radial Magnetic Circuit Parallel Hybrid Excitation Synchronous Motor*, Proceedings of the Chinese Society of Electrical Engineering (in Chinese), vol. 30, no. 36, pp. 53–58 (2010), DOI: 10.13334/j.0258-8013.pcsee.2010.36.009.

[11] Yu S., *Analysis and Design of Claw-Pole Hybrid Excitation Double Salient Motor for Electric Vehicles*, China University of Petroleum (East China) (2020), DOI: 10.27644/d.cnki.gsydu.2020.001053.

[12] Cheng Z.M., *Design, analysis and control of hybrid excited doubly salient stator-permanent-magnet motor*, SCIENCE CHINA Technological Sciences, vol. 53, no. 1, pp. 188–199 (2010), DOI: 10.1007/s11431-009-0357-0.

[13] Shirzad E., Rahideh A., *Analytical Model for Brushless Double Mechanical Port Flux-Switching Permanent Magnet Machines*, IEEE Transactions on Magnetics, vol. 57, no. 10, pp. 1–13 (2021), DOI: 10.1109/TMAG.2021.3104938.

[14] Fukami T., Hayamizu T., Matsui Y., *Steady-State Analysis of a Permanent-Magnet-Assisted Salient-Pole Synchronous Generator*, IEEE Transactions on Energy Conversion, vol. 25, no. 2, pp. 388–388 (2010), DOI: 10.1109/TEC.2010.2047037.

[15] Yldrz E., Güle M., Aydn M., *An Innovative Dual-Rotor Axial-Gap Flux-Switching Permanent-Magnet Machine Topology with Hybrid Excitation*, IEEE Transactions on Magnetics, vol. 54, no. 11, pp. 1–5 (2018), DOI: 10.1109/tmag.2018.2848878.

[16] Gysen B.L.J., Meessen K.J., Paulides J.J.H., *General Formulation of the Electromagnetic Field Distribution in Machines and Devices Using Fourier Analysis*, IEEE Transactions on Magnetics, vol. 46, no. 1, pp. 39–52 (2010), DOI: 10.1109/TMAG.2009.2027598.

[17] Zhu Z.Q., Wu L.J., Xia Z.P., *An Accurate Subdomain Model for Magnetic Field Computation in Slotted Surface-Mounted Permanent-Magnet Machines*, IEEE Transactions on Magnetics, vol. 46, no. 4, pp. 1100–1100 (2010), DOI: 10.1109/TMAG.2009.2038153.

[18] Zhang Y.F., Gao M.L., Wang L., *Study of Electromagnetic Characteristics of Brushless Reverse Claw-Pole Electrically Excited Generators for Automobiles*, Energies, vol. 16, no. 6, pp. 2573–2573 (2023), DOI: 10.3390/EN16062573.

[19] Cao Y., Feng L., Mao R., *Multi-Objective Layered Optimization Design of Axial Magnetic Field Permanent Magnet Memory Motors*, Chinese Journal of Electrical Engineering, vol. 41, no. 6, pp. 1983–1992 (2021), DOI: 10.13334/j.0258-8013.pcsee.201435.

[20] Aleksas S., Jan S., *Rapid Multi-Objective Design Optimization of Switched Reluctance Motors Exploiting Magnetic Flux Tubes*, IET Science, Measurement & Technology, vol. 12, no. 2, pp. 223–229 (2018), DOI: 10.1049/iet-smt.2017.0213.

[21] Liu Y., Song B., Zhou X., *Analysis and Multi-Objective Optimization Design of Radial-Flux Permanent Magnet Motors*, Journal of Motor and Control (in Chinese), vol. 27, no. 9, pp. 1–9 (2023), DOI: 10.15938/j.emc.2023.09.001.

[22] Cao Y., Feng L., *Multi-Objective Optimization Design of Axial Magnetic Field Permanent Magnet Memory Motors Based on Response Surface Methodology*, Journal of Nanjing University of Information Science & Technology (Natural Science Edition), vol. 13, no. 5, pp. 620–627 (2021), DOI: 10.13878/j.cnki.jnuist.2021.05.016.

[23] Muteba M., *Optimization of Air Gap Length and Capacitive Auxiliary Winding in Three-Phase Induction Motors Based on a Genetic Algorithm*, Energies, vol. 14, no. 15, pp. 4407–4407 (2021), DOI: 10.3390/EN14154407.

[24] Petchrompo S., Coit D.W., Brintrup A., Wannakrairot A., Parlikad A.K., *A review of Pareto pruning methods for multi-objective optimization*, Computers & Industrial Engineering (2022), DOI: 10.1016/J.CIE.2022.108022.

[25] Hu X.B., Gu S.H., Zhang C., *Finding all Pareto Optimal Paths by Simulating Ripple Relay Race in Multi-Objective Networks*, Swarm and Evolutionary Computation, vol. 64, no. 1, 100908 (2021), DOI: 10.1016/J.SWEVO.2021.100908.